BaRuO$_3$ coated Ti plate as an efficient and stable electro-catalyst for water splitting reaction in alkaline medium

Alok Pratap Singh, Susanta Ghosh [*]

Integrated Science Education and Research Centre, Siksha Bhavana, Visva-Bharati (A Central University), Santiniketan, 731235, India

ARTICLE INFO

ABSTRACT

Water splitting using an electrochemical device to produce hydrogen fuel is a green and economic approach to solve the energy and environmental crisis. The realistic design of durable electro-catalysts and their synthesis using a simplistic technique is a great challenge to produce hydrogen by water electrolysis. Herein, we report a stable highly active barium ruthenium oxide (BRO) electro-catalysts over Ti plate using a soft chemical method at low temperature. The synthesized material shows facile hydrogen evolution reaction (HER) as well as oxygen evolution reaction (OER) in alkaline medium with over-potentials of 195 mV and 300 mV, respectively at a current density of 10 mA cm^{-2}. The excellent stability lasts for at least 24 h without any degradation for both the HER and OER at the current density of 10 mA cm^{-2}, inferring the practical applications of the material toward production of green hydrogen energy. Certainly, the synthesized catalyst is capable adequately for the overall water splitting at a cell voltage of 1.60 V at a current density of 10 mA cm^{-2} with an impressive stability for at least 24 h, showing a minimum loss of potential. Thus the present work contributes to the rational design of stable and efficient electro-catalysts for overall water splitting reaction in alkaline media.

1. Introduction

With the development of the technologies and growth of the population, the energy demand is increasing across the globe. As a result, usage of fossil fuels as a source of energy has increased significantly, and the resulting CO$_2$ emissions have increased the greenhouse effect [1]. Therefore, it is highly required to develop a sustainable energy source as feasible alternatives to the conventional fossil fuels [2]. Among all existing renewable energy sources, hydrogen has received much interest as a clean energy source [3,4] and thus, the hydrogen production has attracted a broad interest. High-purity, large scale and cost-effective hydrogen can be produced via water electrolysis, which involves two half-cell reactions, i.e., hydrogen evolution reaction at the cathode and oxygen evolution reaction at the anode [5,6]. The water splitting through electrochemical process have unfavorable thermodynamics and sluggish reaction kinetics, so it is highly required to create high-performance electro-catalysts that can lower the activation energy barriers and thus accelerate the reactions [7–9]. Platinum (Pt) is the most effective electro-catalyst for HER with zero onset potential, while RuO$_2$, IrO$_2$ and their composites are efficient for OER due to their rutile crystallographic structure [6,10,11]. Ruthenium and Platinum both are belongs to the noble metal family, while the cost of Ru is much less than the Pt [12]. Also, Ru has excellent water-dissociation abilities having Pt-like hydrogen bond strength [6,13] and Ru – based catalysts can possess good HER activity due to the favorable hydrogen adsorption of Ru [14–16] (see Scheme 1).

---

* Corresponding author.
E-mail address: susanta.ghosh@visva-bharati.ac.in (S. Ghosh).

Numerous studies are being conducted to create electro-catalysts that can catalyze both HER and OER in the same electrolytic medium while considering the overall effectiveness of the electrolysis process [14,17]. A lower efficiency is often obtained when both the electrodes are made out of the same material and put together in a single electrolytic medium to form a symmetric cell for water splitting reaction [18,19]. The pure transition (noble) metals are not much suitable for water splitting due to their lower activity, whereas their oxides are notable for being highly stable because they cannot be further oxidized even under harsh operating conditions [20,21]. Again the high price and limited supply of the precious metals severely limit their practical applications. To reduce the cost without compromising the catalytic capabilities, attempt has been made to synthesize ruthenium (Ru) with other transition metal based oxides as electro-catalysts for HER and OER [6,14]. In literature, there are numerous techniques, such as solid-state method, hydrothermal method, sol-gel method and deposition method, available to synthesize various oxide materials and it was found that the synthetic method and the curing temperature have profound effect on the crystal growth and hence on their catalytic properties [22–33]. Recent report on the low cost synthesis of bimetallic oxides and its coatings over a metal surface shows the hard-corrosion resistance property [34]. Again, the deposition techniques and deposition temperatures have significant impact on their properties, such as oxidation when exposed to air [35–37]. Considering the literature report, we intent to prepare $BaRuO_3$ electro-catalyst using a soft chemical method at low temperature for its use in the water splitting reaction in alkaline medium, though Doggali et al. have already synthesized $BaRuO_3$ perovskite material at high temperature for its use as a catalyst for the diesel soot oxidation [38]. To the best of our knowledge, this is the first report on low temperature synthesis of $BaRuO_3$ for the water splitting reaction in alkaline medium. Advantage of choosing the soft chemical route for the preparation of $BaRuO_3$ on Ti plate is that it does not require the use of an inert atmosphere or any toxic organic solvent. Secondly, the shorter Ru–Ru bond distance in $BaRuO_3$ compared to RuO_2 and the presence of basic Ba in the moiety of $BaRuO_3$ may enhance the catalytic property and thus the BRO may be a promising efficient electro-catalyst for both the HER and OER in alkaline medium.

2. Experimental methodology and techniques

2.1. Materials

Ruthenium (III) Chloride Hydrate ($RuCl_3 \cdot xH_2O$, $\geq$99.98 %) and Ruthenium (IV) Oxide Hydrate ($RuO_2 \cdot xH_2O$) were purchased from Sigma-Aldrich; Titanium Plate (Ti, Grade B) was purchased from aviation metal & alloys, India; 2-Propanol ($\geq$99.0 %), Acetone ($\geq$99.0 %), Hydrochloric Acid (HCl, $\geq$35.0 %), Barium Nitrate ($Ba(NO_3)_2$, $\geq$99 %) and Potassium Hydroxide Pellets (KOH, $\geq$84 %) were purchased from Merck. Carbon black, acetylene (99.9 %) and Nafion D-520 dispersion (5 % w/w in water and 1-propanol) were purchased from Alfa Aesar. All the salts were used without any further purification. Tripled distilled water was prepared using a BOROSIL® distillation unit to make each solution.

2.2. Preparation of $BaRuO_3$ coated Ti plate

Ti plates were scratched with sand paper (250 μm), then cleaned ultrasonically in 20 % of HCl for 15 min to remove the impurities from its surface and washed again with distilled water and acetone. To prepare $BaRuO_3$ solution by soft chemical method, the stoichiometric amounts of $Ba(NO_3)_2$ (0.183 g) and $RuCl_3 \cdot xH_2O$ (0.145 g) were dissolved in 5 ml tripled distilled water separately. $RuCl_3$ solution was heated up at 80 °C for 5 min under constant stirring and then $Ba(NO_3)_2$ solution was added into it drop-by-drop. The whole solution was heated under constant stirring condition at 80 °C for another 10 min to obtain a dark brown solution. The obtained brown solution (ink) was coated on Ti plate with a geometrical area of 1 cm^2 using a soft brush and dried it at 120 °C for 10 min in a hot air oven. This procedure was repeated for another five times to get a reasonable amount of $BaRuO_3$ material over Ti plate and designated as BRO. The obtained BRO was annealed in a muffle furnace at different temperature of 200 °C, 300 °C, 400 °C and 500 °C in the presence of air for 1 h, which were named as BRO-2, BRO-3, BRO-4 and BRO-5, respectively. The active mass of coated $BaRuO_3$ on Ti plate after calcination was~10 mg. A schematic diagram of the whole process is shown below (Scheme 1).
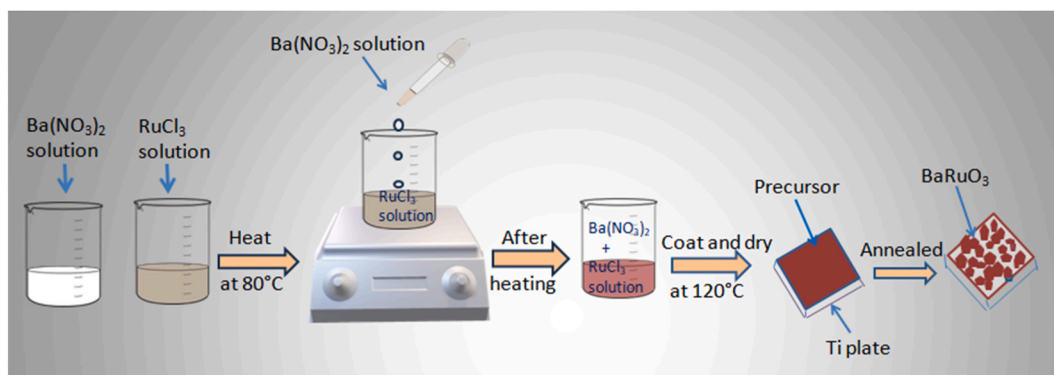
Scheme 1. Schematic illustration of $BaRuO_3$ coated Ti plate.

2.3. RuO$_2$ electrode preparation

For comparison, 12 mg of commercial RuO$_2$ and 3 mg of carbon black were dispersed in 2 μl of Nafion and 250 μl of 2-propanol and untrasonicated for 60 min to obtain a homogeneous dispersion, called ink. The ink, as obtained, was drop-casted on Ti plate with a geometrical area of 1 cm^2 and dried it at room temperature. The process was repeated for another five times to get an active mass of ~10 mg over the Ti plate.

2.4. Physical characterizations

The phase structure and crystallinity of the prepared electrode materials were identified by X-ray diffraction (XRD, PANalytical X'Pert Pro) using Cu-K$_\alpha$ radiation, λ = 1.54059 Å. The surface morphologies of the synthesized BRO electrodes were studied by field emission scanning electron microscopy (FE-SEM, Zeiss Gemini SEM 450). X-ray photoelectron spectroscopy was performed for the analysis of chemical states of the elements present on the surface of BaRuO$_3$ coated Ti plate by using X-ray photoelectron spectrometer (XPS, Thermo Scientific Nexsa G2) equipped with a monochromatic Al-K$_\alpha$ X-ray source.

2.5. Electrochemical characterizations

All electrochemical measurements were performed using an Autolab potentiostat/galvanostat workstation (Model- PGSTAT 128 N) comprising a standard three-electrode cell in 1 M KOH solution (pH = 13.5). The pH of KOH solution was measured by using a pH meter (LABMAN, LMPH-12). Platinum metal plate (2 cm × 1 cm) and a saturated calomel electrode (SCE) were used as counter and reference electrodes, respectively. The BaRuO$_3$ coated Ti plates (1 cm^2) obtained at different temperature were used as working electrode. Linear sweep voltammetry (LSV) curves were recorded at a sweep rate of 5 mV s^{-1} vs. SCE without any iR compensation for the OER and HER. The electrochemical active surface area (ECSA) of the best electrode was calculated by measuring the double-layer capacitance (C$_{dl}$) in the non-faradic region at various scan rates starting from 5 to 50 mV s^{-1} in the potential range of 0.0–0.15 V vs. SCE in 1 M KOH solution according to the reported method. The double layer capacitance (C$_{dl}$) was calculated from the slope of the graph plotted against Δj vs. scan rate, where Δj = j$_{anodic}$ - j$_{cathodic}$/2, and C$_{dl}$ value is equal to the slope value [39,40].

All the potentials recorded against SCE were converted in terms of Reversible Hydrogen Electrode (RHE) calculated by equation (1), and the over-potential was calculated by equation (2) [41]:

$$V_{RHE} = V_{SCE} + 0.059\,pH + 0.2415 \tag{1}$$

$$\eta = V_{RHE} - 1.23 \tag{2}$$

where, V$_{RHE}$ is the Reversible Hydrogen Electrode (RHE) potential, V$_{SCE}$ is the measured potential vs. Saturated Calomel Electrode (SCE), 0.2415 is the standard electrode potential of SCE and η is the over-potential.

Electrochemical impedance spectroscopy (EIS) studies were performed in a frequency range of 0.1 MHz–1 Hz. The long term stability of the best electrode was tested by performing chrono-potentiometry at constant cathodic (for HER) and anodic (for OER) current density of 10 mA cm^{-2}. The stability of the electro-catalysts was studied using a two electrode system in which a platinum plate acts as both counter & reference electrode and BRO-3 coated Ti as working electrode in 1 M KOH solution. Overall water splitting performance was studied using a two electrode system, where both the electrodes were BRO-3 electrodes.
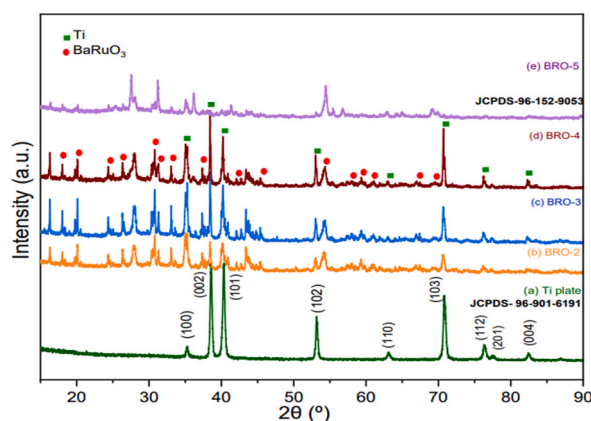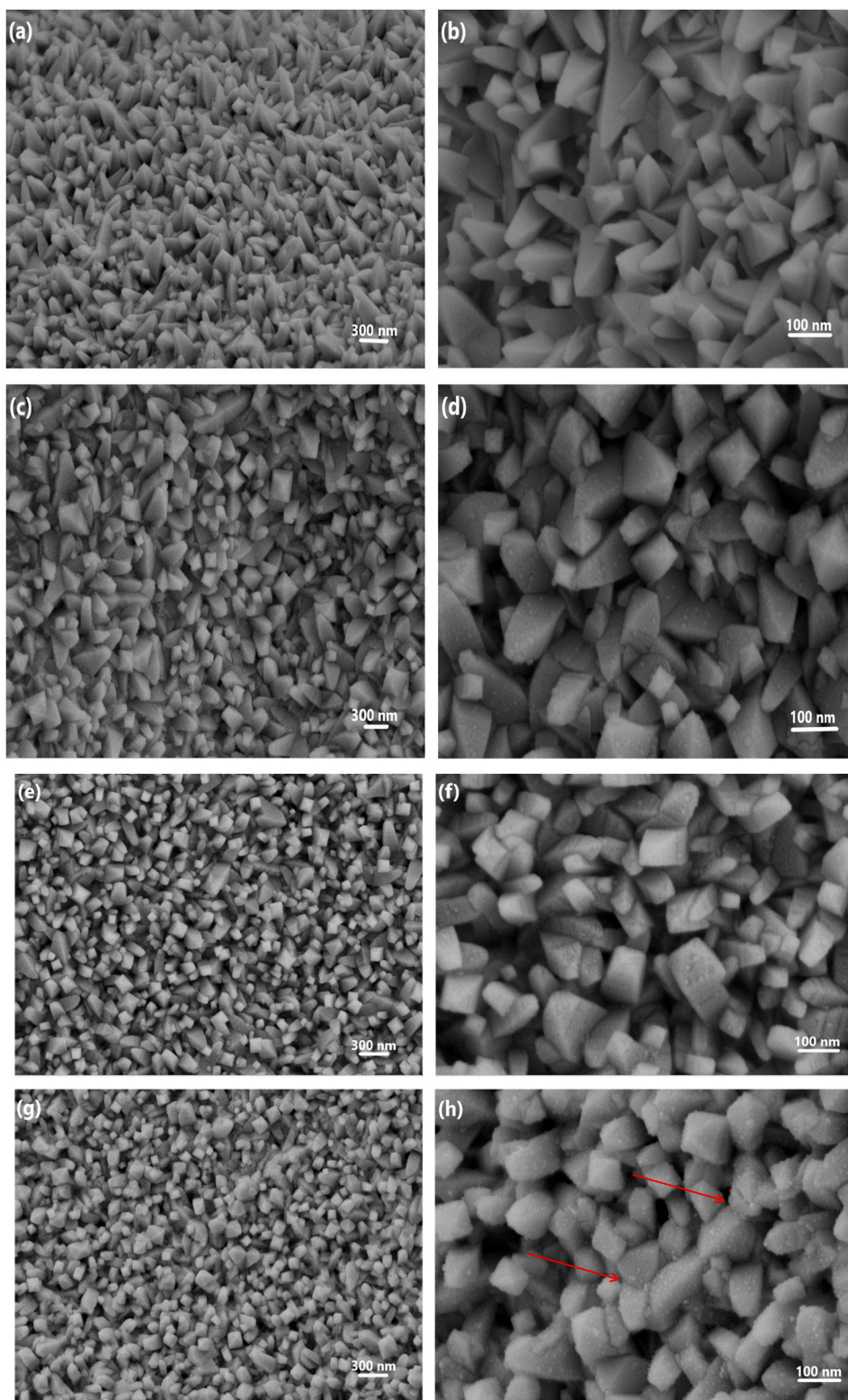

Fig. 1. XRD patterns of (a) Bare Ti plate, (b) BRO-2, (c) BRO-3, (d) BRO-4, and (e) BRO-5.

Fig. 2. FE-SEM images of BRO with different magnification annealed at different temperature (a,b) 200 °C (c,d) 300 °C (e,f) 400 °C and (g, h) 500 °C.

3. Results and discussion

3.1. Composition and morphology analysis

The phase structure of the prepared BRO materials and the Ti plate were studied by XRD. Fig. 1 (a) reveals the XRD patterns of bare Ti plate with the diffraction peaks at a 2θ values of 35.10°, 38.44°, 40.18°, 53.03°, 62.97°, 70.70°, 76.24°, 77.38°, and 82.35° correspond to (100), (002), (101), (102), (110), (103), (112), (201), and (004) planes, matched well with the standard JCPDS data (Card No.- 96-901-6191) and confirmed that no other impurities are present in the Ti plate. Fig. 1(b–e) show the XRD pattern of BRO materials annealed at different temperatures. Fig. 1 (b) shows the XRD pattern of BRO-2 films annealed at 200 °C contains both stoichiometric and non-stoichiometric phases like $Ba_7Ru_4O_{15}Cl_2$. Formation of non-stoichiometric phase is common for materials synthesized from solution at low temperature. Fig. 1(c and d) show the XRD pattern of the films annealed at 300 °C & 400 °C with diffraction lines at 2θ values of 17.91°, 19.96°, 24.25°, 26.31°, 30.65°, 31.21°, 32.91°, 35.35°, 37.05°, 40.63°, 42.51°, 45.34°, 50.23°,
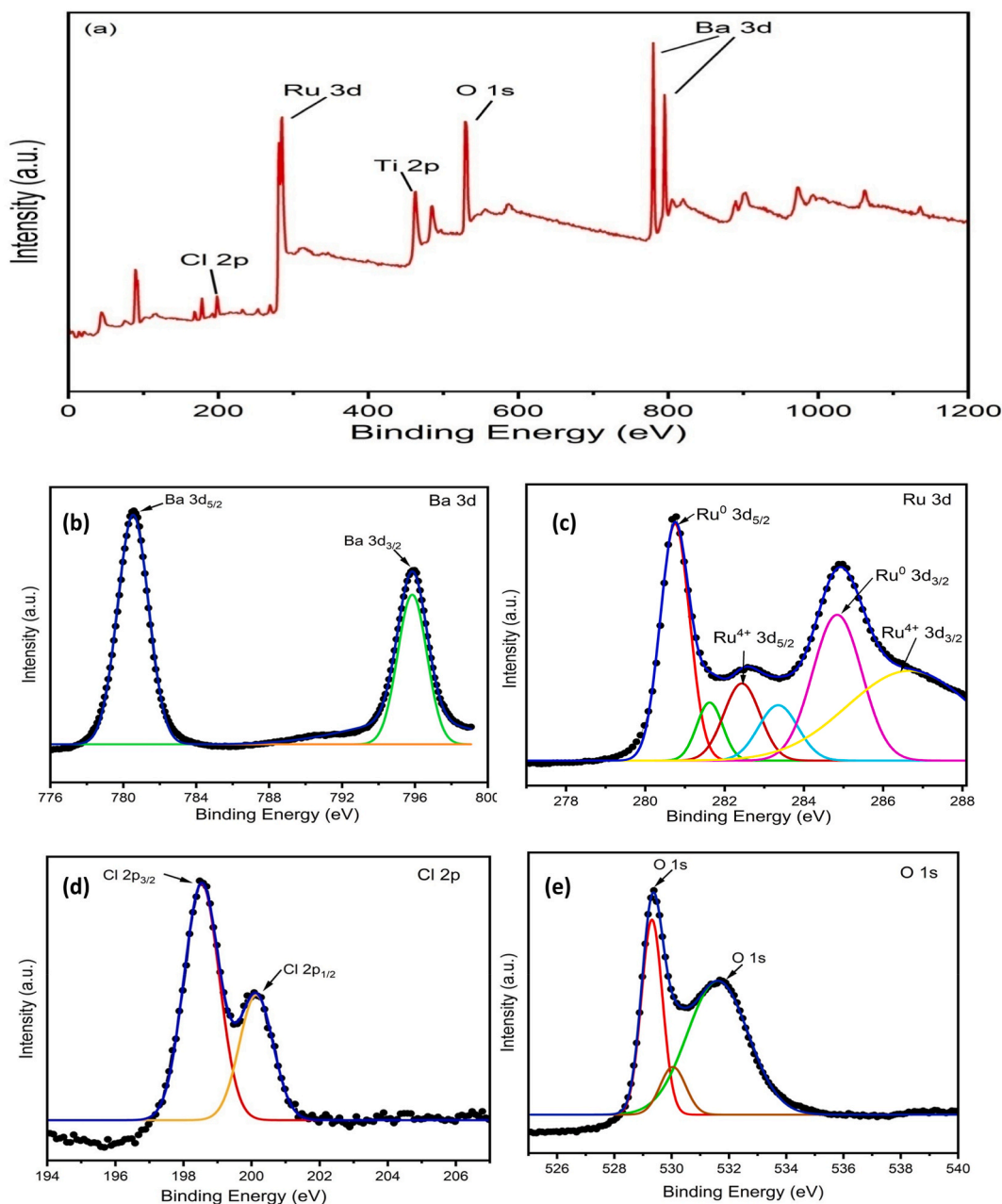

Fig. 3. XPS survey spectrum of BRO-3 (a) Full XPS spectra, and high-resolution XPS spectra of (b) Ba 3d, (c) Ru 3d, (d) Cl 2p, and (e) O 1s.

54.00°, 57.39°, 59.27°, 61.90°, 66.80°, 69.44°, and 73.96° with an intense peak at 31.21° corresponds to the (110) plane of $BaRuO_3$, which matches well with the standard JCPDS data (Card No.- 96-152-9053) and confirms the formation of hexagonal perovskite structure. The average crystalline size of the synthesized materials were determined by using the well known Scherrer equation: $D = k\lambda/(\beta \cos\theta)$, where, D is the average crystalline size, λ is the wavelength of X-ray (1.54059 Å), k is the shape factor (0.9), β is the full width at half-maximum of the peak in radian, and θ is the Bragg angle of the (hkl) reflection [42]. The average crystalline sizes of BRO-2, BRO-3, and BRO-4 are 87.25 nm, 118.3 nm, and 115.23 nm, respectively measured using the (110) reflection plane at $2\theta =$ 31.21°. It should be mentioned here that BRO-5 annealed at 500 °C didn't show a large number of sharp peaks in the diffraction pattern, which indicates that there is a change in the crystal structure at and above 500 °C. This change can be attributed due to a permanent chemical reaction between BRO and TiO_2 to form a solid solution, when annealed at 500 °C. It is reported that the parabolic oxidation of titanium metal takes place above 500 °C governed by the dissolution of oxygen in the titanium metal [43] and thus forming a thick oxide layer over pure Ti metal. As a result the diffraction lines of the pure Ti metal disappeared at 500 °C.

The surface morphologies of the BRO materials, synthesized at different temperatures, were investigated by FE-SEM. The morphology of the BRO films over Ti plate shows closely packed pyramidal shaped particles that are 70–123 nm in diameter and more than 100 nm in length, shown in Fig. 2(a–h). The magnified images clearly show that particles are well separated from each other and each pyramidal shaped particle is exposed to the air. Between particles there is an empty space which is essential for efficient functioning of a catalyst, particularly in surface catalysed reactions. Again a careful screening shows that the crystal growth initiates at 200 °C and uniform pyramidal shaped particles are developed throughout the surface at 300 °C. However, the morphology has changed from a sharp pyramid to a fused one at 500 °C, shown by an arrow in Fig. 2 (h), which is also confirmed from the XRD pattern. This indicates that there is a phase transition around 500 °C.

The elemental oxidation states of BRO-3, as representative case, were also analyzed by the XPS technique and the result for the wide scan spectrum is shown in Fig. 3(a). Considering the literature data and the position of the binding energies of the synthesized materials, it is confirmed that BRO-3 sample contains Ba, Ru and O elements with a trace amount of Cl on the surface of the synthesized electrode. Fig. 3(b) shows the deconvoluted high-resolution XPS spectra of Ba 3d; the peak at 780.58 and 795.88 eV are assigned to the main peak of Ba $3d_{5/2}$ and Ba $3d_{3/2}$ corresponding to the Ba^{2+} state [44,45]. Hence, it was confirmed that barium is present in the BRO-3 lattice as Ba^{2+} states. The high resolution deconvoluted XPS spectrum of Ru 3d is shown in Fig. 3(c), which is much more complex and six components were necessary to find a fit of high accuracy. The peaks at 280.78 and 284.98 eV, with a spin-orbital coupling separation of 4.20 eV, are assigned to the metallic peaks of Ru^o $3d_{5/2}$ and Ru^o $3d_{3/2}$, respectively. The peaks presented at 282.42 eV and 286.72 eV are associated with Ru^{4+} $3d_{5/2}$ and Ru^{4+} $3d_{3/2}$ oxidation state whereas the peaks at 281.55 and 283.34 eV
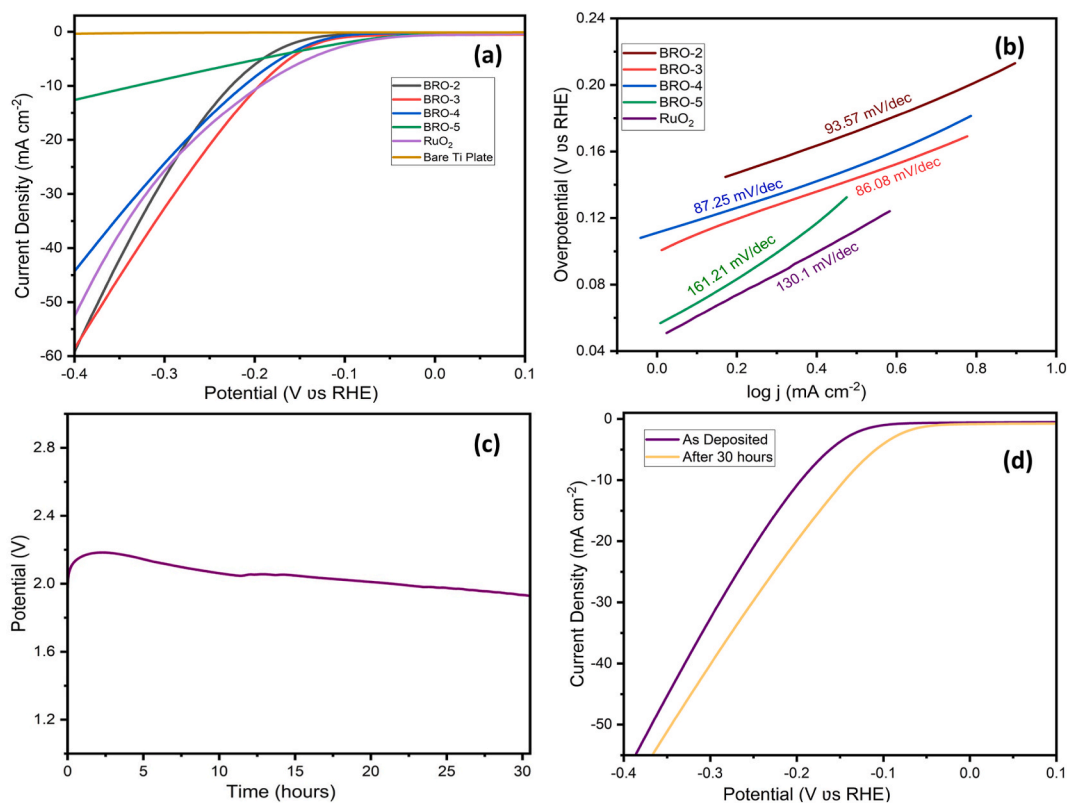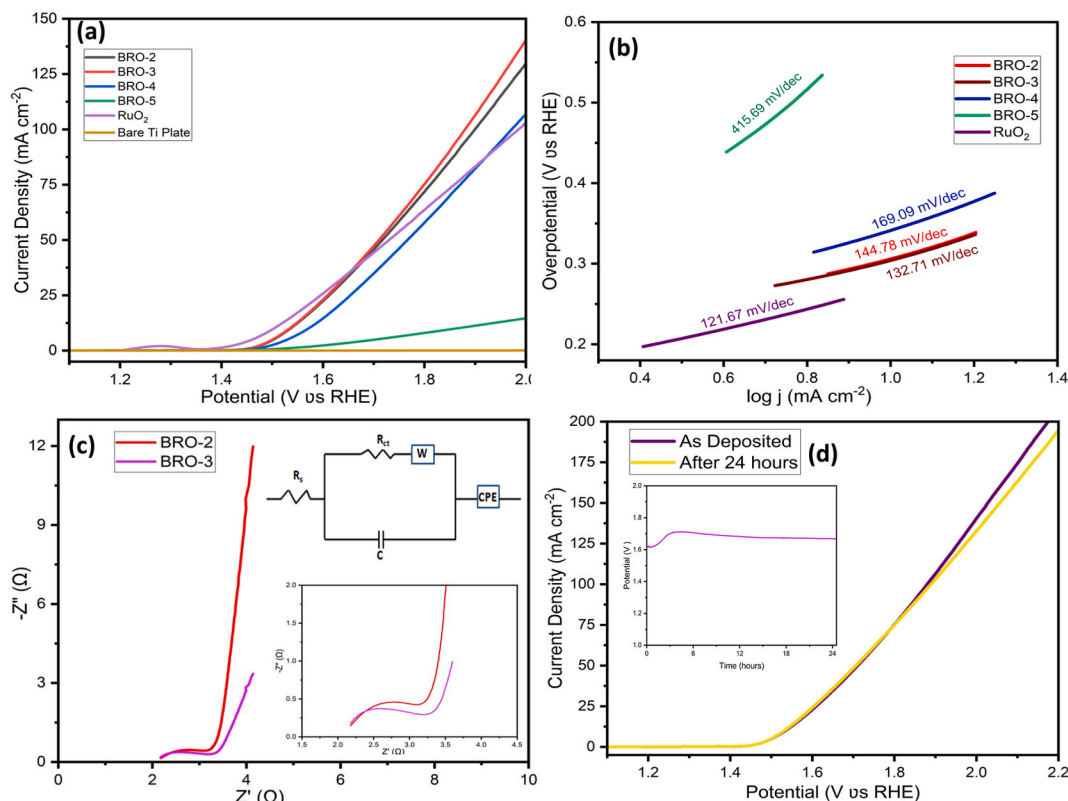

Fig. 4. Electrochemical studies of BRO annealed at different temperatures for HER (a) LSV curves at 5 mV s^{-1} scan rate, (b) Tafel plots, (c) Long-term stability test at j = 10 mA cm^{-2} of BRO-3, and (d) Comparison of LSV curves before and after stability test of BRO-3.

correspond to the satellite peaks of Ru^{4+} $3d_{5/2}$ [46,47]. The deconvoluted XPS spectrum of Cl 2p shown in Fig. 3(d) have two peaks at 198.48 and 200.08 eV which belonged to Cl $2p_{3/2}$ and Cl $2p_{1/2}$ respectively, indicating the existence of Cl^- state [48,49] in BRO-3. Trace amount of chloride ions is present in the non-stoichiometric BRO as expected due to the solution phase synthesis at low temperature using chloride precursor. The presence of chloride ions in the lattice site of the catalyst might have adverse effect in catalytic activity, when metal-oxygen linkage is very important. When some of the oxygen sites are occupied by the chlorine atoms, the number of active sites is reduced to some extent and thus activity diminishes. Similar phenomenon was also observed on the catalytic performance of Co_3O_4 for CO oxidation [50]. Thus it is desirable to synthesize a phase pure BRO material free from chloride ions for better performance. The high resolution XPS spectrum for O 1s, shown in Fig. 3(e), shows two peaks, one is very sharp and another is broad. The whole spectrum is deconvolated into three peaks with binding energies at 529.38, 530.01 and 531.68 eV, respectively. The peak at 529.38 eV and 531.68 eV were assigned to the lattice oxygen in the metal oxide framework under different chemical environments, whereas the peak with low intensity at 530.01 eV was assigned to the OH^- groups, due to adsorbed water from the environment and it is very common for metal oxides [51].

3.2. HER analysis

The electro-catalytic properties of the as-prepared BRO electrodes over Ti Plate were tested for the HER in 1 M KOH solution by using a standard three electrode systems without any iR compensation and compared with commercial RuO_2 electro-catalyst, where the mass loading of the electro-catalysts in each electrode was approximately 10 mg. The HER activity, if any, of the pure Ti plate of area 1 cm^2 was also tested under the same experimental conditions. Fig. 4(a) shows the HER activities of BRO-2, BRO-4, BRO-5, RuO_2 and bare Ti plate, recorded using LSV technique at a scan rate of 5 mV s^{-1} between −0.1 V and −1.4 V vs. SCE, which is converted with respect to RHE. As shown in Fig. 4(a), BRO-3 electrode showed the lowest over-potential (η_{10}) of 195 mV vs. RHE to deliver a current density of 10 mA cm^{-2}, whereas BRO-2, BRO-4, BRO-5 and RuO_2 electrodes were showing over-potentials (η_{10}) of 227 mV, 213 mV, 332 mV, and 195 mV, respectively to afford the same current density of 10 mAcm^{-2}. BRO-3 shows the highest HER performance compared to the other synthesized electrodes, while bare Ti plate electrode shows no HER activity in 1 M KOH. But it was notable that the HER activity of BRO-3 increases and surpasses RuO_2 as the over-potential exceeds 200 mV. This can be explained in terms of formation of large pyramidal shaped open structure at 300 °C in case of BRO-3. The HER kinetics was determined by plotting Tafel curves which were recorded with the linear portions of the polarization curve at low over-potential region fitted to the Tafel equation

Fig. 5. Electrochemical studies of BRO annealed at different temperatures for OER (a) LSV curves at 5 mV s^{-1} scan rate, (b) Tafel plots, (c) Nyquist plots of electrochemical impedance spectra of BRO-2 and BRO-3 for OER process, and (d) Comparison of LSV curves before and after stability test. The inset picture shows chrono potentiometric test of BRO-3 at 10 mA cm^{-2} for 24 h.

(η = b log |j| + a, where η = over-potential, j = measured current density and b = Tafel slope and a = constant, related to the equilibrium exchange current density). Fig. 4(b) shows the Tafel plots for BRO-2, BRO-3, BRO-4, BRO-5 and RuO_2 electrodes with Tafel slopes of 93.57, 86.08, 87.25, 161.21, and 130.1 mV dec^{-1}, respectively. The low Tafel slope value of 86.08 mVdec^{-1}confirmed the favorable HER over BRO-3 surface. The smaller Tafel slope means faster the HER reaction, proceeding via the Volmer-Heyrovsky mechanism [52,53]. For the practical applications of the electro-catalyst, the stability and durability, which are the critical factors, were tested after assembling a two electrode cell in 1 M KOH solution in which a platinum plate acts as counter as well as reference electrode and BRO-3 as working electrode. Fig. 4(c) displayed the chrono-potentiometric test of BRO-3 at constant current density of 10 mA cm^{-2} for more than 30 h without any iR compensation. Initially, the potential value of BRO-3 electrodes increases because the diffusion layer near the electrode surface exhausted and looking for another layer to maintain the current density of 10 mA cm^{-2}. But after 2.5 h, the potential starts decreasing and finally attains the starting potential around 30 h and remains constant. At this point, the double layer charging is completed and almost all the current is passing through the double layer to do the faradaic process. In order to confirm the phase changes, if any, the LSV curve for the electrode that has completed 30 h contineous electrolysis was recored at the same scan rate of 5 mV s^{-1} and compared with the result recorded for the same electrode before the stability test, as shown in Fig. 4(d). From the graph, it was found that there is a drop in overpotential (η_{10}) (from 195 to 144 mV) value without comprmising its catalytic activity and thus it confirmed that BRO-3 material is not only very stable, but also improves its charge transfer kinetics due to the formation of uniform channel structure during long-term electrolysis in alkaline medium. The stability test keep showing better performance with respect to time in alkaline media and thus confirmed that $BaRuO_3$ is a stable and efficient electro-catalyst for the hydrogen evolution reaction (HER).

3.3. OER analysis

The OER activities of BRO-2, BRO-3, BRO-4, BRO-5, RuO_2 and bare Ti plate electrodes were also tested and compared in 1 M KOH solution at a scan rate of 5 mV s^{-1} by using a three electrode system without any iR compensation, shown in Fig. 5(a). Very similar activities were found at~1.5 V for the BRO-2 and BRO-3 electrodes, with η_{10} of 310 and 300 mV, respectively, whereas commercial RuO_2 needs an over-potential of 275 mV to achieve the same current density of 10 mA cm^{-2}. It is interesting to note that the LSV curves of BRO-2 and BRO-3 surpassed the RuO_2 curve after 1.66 V with rapid evolution of oxygen. Again, the LSV curve of BRO-3 surpassed the BRO-2 curve after 1.75 V with rapid evolution of oxygen, with the over-potentials of 670 and 650 mV for BRO-2 and BRO-3, respectively, to achieve the current density of 100 mA cm^{-2}. BRO-4, and BRO-5 need over-potentials of 340, and 630 mV to achieve current density of 10 mA cm^{-2}, respectively, where bare Ti plate showing no response at all. By plotting the corresponding Tafel plots of all the electrodes shown in Fig. 5(b), it was found that BRO-3 also show the most favorable kinetics reaction with a Tafel slope of 132.71 mV dec^{-1} which is smaller than that of BRO-2 (144.78 mV dec^{-1}), BRO-4 (169.09 mV dec^{-1}), BRO-5 (415.69 mV dec^{-1}), and RuO_2 (121.67 mV dec^{-1}), respectively. BRO material has dual advantages towards oxygen evolution; firstly because of the direct Ru–Ru interaction as compared to pure RuO_2 favours the dissociative adsorption of oxygen. Secondly the presence of basic Ba cation in BRO matrix can weaken the strength of the Ru–O bond and thus facilitates the release of oxygen [38]. To further unravel the mechanism of OER kinetics, electrochemical impedance spectroscopy (EIS) was recorded in 1 M KOH solution under open voltage without any iR compensation. The Nyquist plots of the BRO-2 and BRO-3 electrodes recorded in the frequency region of 0.1 MHz–1 Hz with a magnified view in the higher frequency region is shown in Fig. 5(c). It is found that the plot has a semicircle at high to medium frequency region and rises sharply at low frequency region. The diameter of the semicircle indicates the charge transfer resistance (R_{ct}) and the slope of the straight line at low frequency region represent the diffusive resistance of the electrolyte to the electrode surface. The smaller semicircle indicating smaller charge transfer resistance (R_{ct}), related to faster interfacial kinetics [54]. The magnified view, shown in inset of Fig. 5(c), shows that BRO-3 has smaller semicircle than BRO-2, suggesting BRO-3 has better electronic conductivity and thus better charge transfer kinetics at the interface. The observed charge transfer resistance (R_{ct}) for BRO-3 is 770 mΩ, which is
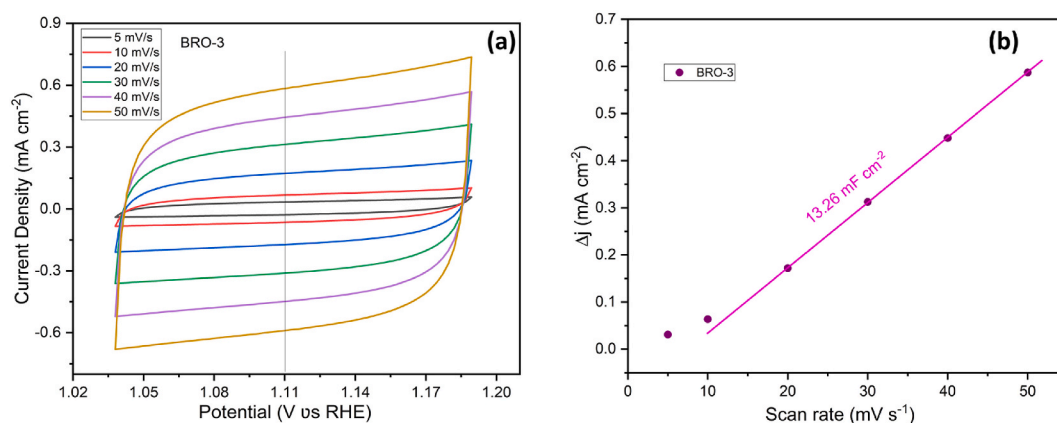

Fig. 6. ECSA studies of BRO-3 in 1 M KOH (a) CV measured in non-faradic region at different scan rates, and (b) C_{dl} measurement graph.

smaller than BRO-2 (855 mΩ) and the corresponding equivalent circuit was shown in Fig. 5(c). To probe the stability of the BRO-3 electrode, towards OER, the chronopotentiometric test was performed by using a two electrode set-up, in which a platinum plate (2 cm × 1 cm) was used as counter as well as reference electrode and BRO-3 was used as working electrode in the 1 M KOH. The long-term stability test for the BRO-3 electrode was determined over 24 h under a constant current density of 10 mA cm^{-2} shown in inset of Fig. 5(d). In the beginning, the potential value has increased to find another diffusion layer, when the layer near the electrode surface exhausted, to maintain the desired current. It decreases slowly and attains the steady value of 1.6 V after 12 h of the test and then it remains almost constant. The decomposition potential at a current density of 10 mA cm^{-2}, in case of chronopotentiometric experiment, is slightly higher than the LSV experiment and this is because of the use of two electrode systems, where platinum (Pt) acts as both the counter and reference electrode. Fig. 5(d) shows the LSV curve before and after 24 h of continuous OER. The curves are nearly overlapping indicating the excellent catalytic durability of BRO-3 material. The electrochemical active surface area (ECSA) of BRO-3 electrode was also determined by measuring the double layer capacitance (C_{dl}) to further evaluate the catalytic activity. The non-faradic current range under different scan rates (5–50 mV s^{-1}) for the BRO-3 electrode was measured as shown in Fig. 6(a). By plotting a graph between capacitive currents Δj and the scan rate yields a straight line as shown in Fig. 6(b). C_{dl} value of BRO-3 was determined from the slope value of the straight line. The ECSA of the BRO-3 was further calculated using the given equation: ECSA = C_{dl}/C_s, where C_s is the specific capacitance value, which is 0.040 mF cm^{-2} in 1 M KOH solution based on previously published reports [55,56]. The calculated ECSA value of the BRO-3 is 331.5 cm^2.

In order to ascertain the significance of the present study, a comparative study has been carried out using ruthenium based composite materials (Table 1) for which electrochemical water electrolysis was carried out in alkaline medium though there is no report on the present material. From the table it is clear that pure RuO$_2$ and its composite material show higher catalytic activity compared to BRO-3 towards HER, but the OER activity of the BRO material is either comparable or higher compared to the reported materials. The better catalytic activity of BRO-3 can be explained on the basis of direct Ru–Ru interaction in BRO as compared to pure RuO$_2$ favours the dissociative adsorption of oxygen. Secondly the presence of basic Ba cation in the BRO matrix can weaken the strength of the Ru–O bond and thus facilitates the release of oxygen [38]. Since the BRO-3 material is very stable for both the HER and OER, it is worthwhile to assemble a symmetric cell using BRO-3 material for the overall water splitting reaction.

3.4. Overall water splitting

Based on the above results, where BRO-3 shows an excellent OER and HER activities as well as stability, a symmetric cell using BRO-3 material as anode as well as cathode was assembled in 1 M KOH solution. For comparison purposes, another cell with BRO-3 as anode and Bare Ti plate as cathode were also assembled. Fig. 7(a) shows the LSV response of both the cell and it was found that the symmetric cell, BRO-3(+)/BRO-3(−), exhibited outstanding performance for the overall water splitting with a cell voltage of 1.65 V to reach a current density of 10 mA cm^{-2}, while BRO-3(+)/Bare Ti plate (−) required cell voltage of 2.25 V to achieve the same current density of 10 mA cm^{-2}. For the stability study, the chronopotentiometry test was performed at a current density of 10 mA cm^{-2} for 24 h, shown in the inset of Fig. 7(b) and it was found that there is no potential loss during 24 h at the current density of 10 mA cm^{-2}. After conteneous electrolysis for 24 h, the LSV curve was recorded using the same set-up, BRO-3(+)/BRO-3(−) and compared with the LSV curve obtained before the stability test as sown in Fig. 7(b). From the figure, it was found that the cell performance enhanced with respect to time and there is potential drop from 1.65 V to 1.60 V to achieve the current density of 10 mA cm^{-2} after 24 h of stability test. All these results demonstrated the remarkable stability and good durability of BRO-3 for overall water splitting.

4. Conclusions

A simplistic and realistic synthetic strategy has been developed to prepare a binder free pyramidal shaped BaRuO$_3$ (BRO) electro-catalyst over Ti plate. The synthesized BaRuO$_3$, annealed at 300 °C, demonstrate remarkable catalytic activity, favorable kinetics, and excellent durability for both the OER and HER under alkaline conditions. A symmetric cell using BRO-3 electro-catalysts was assembled which shows an overall water splitting voltage 1.60 V, equal to the benchmark standards in water splitting reaction, to achieve a current density of 10 mA cm^{-2}. A permanent phase and morphology change of BaRuO$_3$ over Ti plate were observed at 500 °C. Thus, the present strategy endorses the development of a binder free electro-catalyst at low temperature, at 300 °C, with high stability and high activity in alkaline medium, demonstrating its viability for wide range of applications of clean energies; such as water

Table 1
Comparison of HER and OER activity results of previously reported related works.

Catalysts	Electrolyte	HER Overpotential (mV) at 10 mA/cm^2	OER Overpotential (mV) at 10 mA/cm^2	References
BRO-3	**1 M KOH**	**195**	**300**	**This Work**
IrO$_2$–RuO$_2$/C	1 M KOH	75	270	[57]
Ru/RuO$_2$–MoO$_2$	1 M KOH	18	260	[58]
Ru/NF-2	1 M KOH	10	330	[59]
RuTe$_2$	1 M KOH	34	275	[60]
Ru–TiO$_2$	1 M KOH	150	–	[61]
1-RuO$_2$/CeO$_2$	1 M KOH	–	350	[62]
RuO$_2$/Co3O$_4$ - MOF	1 M KOH	89	305	[63]
Rh$_{50}$Ru$_{50}$@UiO-66- NH$_2$	1 M KOH	176	–	[64]
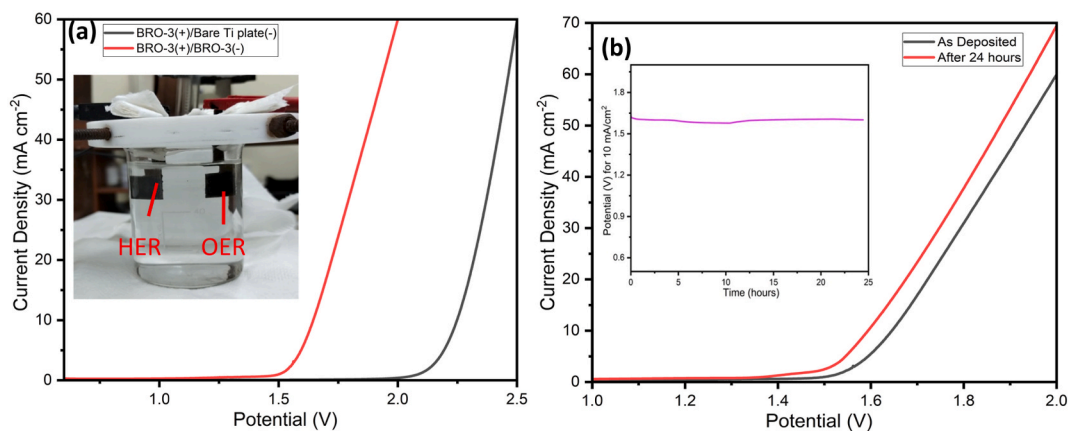
Fig. 7. Overall water-splitting performance (a) BRO-3/Bare Ti plate and BRO-3/BRO-3 in a two-electrode alkaline solution at the scan rate of 5 mV s^{-1}. The inset photo shows the H_2 and O_2 bubbles on the electrodes, (b) Comparison of LSV curves before and after stability test of BRO-3/BRO-3. The inset shows chrono potentiometric test of BRO-3/BRO-3 at 10 mA cm^{-2} for 24 h.

electrolyser, metal-air battery, etc.

Author contribution

Alok Pratap Singh: Performed the experiments; Analyzed and interpreted the data; Wrote the paper.
Susanta Ghosh: Conceived and designed the experiments; Analyzed and interpreted the data; Wrote the paper.

Funding statement

Data availability

Data will be made available on request.

Declaration of competing interest

The authors declare that they have no known competing financial interests or personal relationships that could have appeared to influence the work reported in this paper.

Acknowledgements

References

[1] A.M. Omer, Energy, environment and sustainable development, Renew. Sustain. Energy Rev. 12 (2008) 2265–2300, https://doi.org/10.1016/j.rser.2007.05.001.
[2] J. Tian, Q. Liu, A.M. Asiri, X. Sun, Self-supported nanoporous cobalt phosphide nanowire arrays: an efficient 3D hydrogen-evolving cathode over the wide range of pH 0–14, J. Am. Chem. Soc. 136 (2014) 7587–7590, https://doi.org/10.1021/ja503372r.
[3] M.S. Dresselhaus, I.L. Thomas, Alternative energy technologies, Nature 414 (2001) 332–337, https://doi.org/10.1038/35104599.
[4] N.S. Lewis, D.G. Nocera, Powering the planet: chemical challenges in solar energy utilization, Proc. Natl. Acad. Sci. U.S.A. 103 (2006) 15729–15735, https://doi.org/10.1073/pnas.0603395103.
[5] Y. Du, H. Qu, Y. Liu, Y. Han, L. Wang, B. Dong, Bimetallic CoFeP hollow microspheres as highly efficient bifunctional electrocatalysts for overall water splitting in alkaline media, Appl. Surf. Sci. 465 (2019) 816–823, https://doi.org/10.1016/j.apsusc.2018.09.231.
[6] Y. Lin, M. Zhang, L. Zhao, L. Wang, D. Cao, Y. Gong, Ru doped bimetallic phosphide derived from 2D metal organic framework as active and robust electrocatalyst for water splitting, Appl. Surf. Sci. 536 (2021), 147952, https://doi.org/10.1016/j.apsusc.2020.147952.
[7] P. Kuang, M. He, H. Zou, J. Yu, K. Fan, 0D/3D MoS$_2$-NiS$_2$/N-doped graphene foam composite for efficient overall water splitting, Appl. Catal. B Environ. 254 (2019) 15–25, https://doi.org/10.1016/j.apcatb.2019.04.072.
[8] S. Riyajuddin, K. Azmi, M. Pahuja, S. Kumar, T. Maruyama, C. Bera, K. Ghosh, Super-hydrophilic hierarchical Ni-foam-graphene-carbon nanotubes-Ni$_2$P–CuP$_2$ nano-architecture as efficient electrocatalyst for overall water splitting, ACS Nano 15 (2021) 5586–5599, https://doi.org/10.1021/acsnano.1c00647.
[9] D. Chinnadurai, R. Rajendiran, O.L. Li, K. Prabakar, Mn-Co bimetallic phosphate on electrodeposited PANI nanowires with composition modulated structural morphology for efficient electrocatalytic water splitting, Appl. Catal. B Environ. 292 (2021), 120202, https://doi.org/10.1016/j.apcatb.2021.120202.

[10] W.H. Hu, X. Shang, J. Xue, B. Dong, J.Q. Chi, G.Q. Han, Y.R. Liu, X. Li, K.L. Yan, Y.M. Chai, C.G. Liu, Activating MoS_2/CNs by tuning (001) plane as efficient electrocatalysts for hydrogen evolution reaction, Int. J. Hydrogen Energy 42 (2017) 2088–2095, https://doi.org/10.1016/j.ijhydene.2016.10.145.

[11] Y. Wu, Y. Li, M. Yuan, H. Hao, X. San, Z. Lv, L. Xu, B. Wei, Operando capturing of surface self-reconstruction of Ni_3S_2/$FeNi_2S_4$ hybrid nanosheet array for overall water splitting, Chem. Eng. J. 427 (2022), 131944, https://doi.org/10.1016/j.cej.2021.131944.

[12] Y. Zheng, Y. Jiao, Y. Zhu, L.H. Li, Y. Han, Y. Chen, M. Jaroniec, S.-Z. Qiao, High electrocatalytic hydrogen evolution activity of an anomalous ruthenium catalyst, J. Am. Chem. Soc. 138 (2016) 16174–16181, https://doi.org/10.1021/jacs.6b11291.

[13] S. Higgins, Regarding ruthenium, Nat. Chem. 2 (2010) 1100, https://doi.org/10.1038/nchem.917, 1100.

[14] J. Liu, Y. Zheng, Y. Jiao, Z. Wang, Z. Lu, A. Vasileff, S.Z. Qiao, NiO as a bifunctional promoter for RuO_2 toward superior overall water splitting, Small 14 (2018), 1704073, https://doi.org/10.1002/smll.201704073.

[15] X. Kong, K. Xu, C. Zhang, J. Dai, S. Norooz Oliaee, L. Li, X. Zeng, C. Wu, Z. Peng, Free-standing two-dimensional Ru nanosheets with high activity toward water splitting, ACS Catal. 6 (2016) 1487–1492, https://doi.org/10.1021/acscatal.5b02730.

[16] J. Greeley, M. Mavrikakis, Surface and subsurface hydrogen: adsorption properties on transition metals and near-surface alloys, J. Phys. Chem. B 109 (2005) 3460–3471, https://doi.org/10.1021/jp046540q.

[17] L. Yan, B. Zhang, J. Zhu, Y. Li, P. Tsiakaras, P. Kang Shen, Electronic modulation of cobalt phosphide nanosheet arrays via copper doping for highly efficient neutral-pH overall water splitting, Appl. Catal. B Environ. 265 (2020), 118555, https://doi.org/10.1016/j.apcatb.2019.118555.

[18] D. Wang, J. Li, Y. Zhao, H. Xu, J. Zhao, Bifunctional Cu_2S–$Co(OH)_2$ nanotube array/Cu foam electrocatalyst for overall water splitting, Electrochim. Acta 316 (2019) 8–18, https://doi.org/10.1016/j.electacta.2019.05.118.

[19] S. Shit, S. Bolar, N.C. Murmu, T. Kuila, Binder-free growth of nickel-doped iron sulfide on nickel foam via electrochemical deposition for electrocatalytic water splitting, ACS Sustain. Chem. Eng. 7 (2019) 18015–18026, https://doi.org/10.1021/acssuschemeng.9b04882.

[20] T. Audichon, T.W. Napporn, C. Canaff, C. Morais, C. Comminges, K.B. Kokoh, IrO_2 coated on RuO_2 as efficient and stable electroactive nanocatalysts for electrochemical water splitting, J. Phys. Chem. C 120 (2016) 2562–2573, https://doi.org/10.1021/acs.jpcc.5b11868.

[21] A.G. Vidales, L. Dam-Quang, A. Hong, S. Omanovic, The influence of addition of iridium-oxide to nickel-molybdenum-oxide cathodes on the electrocatalytic activity towards hydrogen evolution in acidic medium and on the cathode deactivation resistance, Electrochim. Acta 302 (2019) 198–206, https://doi.org/10.1016/j.electacta.2019.02.030.

[22] G. Fraid, Optical properties of ZnO nanorods for reduced graphene oxide, Exp. Theo. Nanotechnology (2023) 449–460, https://doi.org/10.56053/7.3.451.

[23] J. Robin, K. Kelvin, Charge transfer in copper oxide nanostructure, Exp. Theo. Nanotechnology (2023) 325–336, https://doi.org/10.56053/7.2.325.

[24] J. Plain, M. Tréguer-Delapierre, Structural analysis and characterization of lead oxide, Exp. Theo. Nanotechnology (2022) 453–472, https://doi.org/10.56053/6.4.453.

[25] Y. Al-Douri, K. Gherab, K.M. Batoo, E.H. Raslan, Detecting the DNA of dengue serotype 2 using aluminium nanoparticle doped zinc oxide nanostructure: synthesis, analysis and characterization, J. Mater. Res. Technol. 9 (2020) 5515–5523, https://doi.org/10.1016/j.jmrt.2020.03.076.

[26] A. Bouhemadou, D. Allali, K. Boudiaf, B. Al Qarni, S. Bin-Omran, R. Khenata, Y. Al-Douri, Electronic, optical, elastic, thermoelectric and thermodynamic properties of the spinel oxides $ZnRh_2O_4$ and $CdRh_2O_4$, J. Alloys Compd. 774 (2019) 299–314, https://doi.org/10.1016/j.jallcom.2018.09.338.

[27] A. Bouhemadou, O. Boudrifa, N. Guechi, R. Khenata, Y. Al-Douri, Ş. Uğur, B. Ghebouli, S. Bin-Omran, Structural, elastic, electronic, chemical bonding and optical properties of Cu-based oxides ACuO (A=Li, Na, K and Rb): an ab initio study, Comput. Mater. Sci. 81 (2014) 561–574, https://doi.org/10.1016/j.commatsci.2013.09.011.

[28] M.E. Amine Monir, H. Baltach, A. Abdiche, Y. Al-Douri, R. Khenata, S.B. Omran, X. Wang, D.P. Rai, A. Bouhemadou, W.K. Ahmed, C.H. Voon, Doping-induced half-metallic ferromagnetism in vanadium and chromium-doped alkali oxides K_2O and Rb_2O: ab initio method, J. Supercond. Nov. Magnetism 30 (2017) 2197–2210, https://doi.org/10.1007/s10948-017-4021-9.

[29] A. Luis, T. Mauricio, Analysis and characterization of molybdenum-doped cadmium oxide, Exp. Theo. Nanotechnology (2021) 157–162, https://doi.org/10.56053/5.2.157.

[30] S. Sagadevan, S. Vennila, A.R. Marlinda, Y. Al-Douri, M. Rafie Johan, J. Anita Lett, Synthesis and evaluation of the structural, optical, and antibacterial properties of copper oxide nanoparticles, Appl. Phys. A 125 (2019) 1–9, https://doi.org/10.1007/s00339-019-2785-4.

[31] G. Arora, I. Hiroya, Annealing temperature effect on structural properties of tin oxide nanoparticles, Exp. Theo. Nanotechnology (2022) 39–46, https://doi.org/10.56053/6.1.39.

[32] P. Flora, S. Lía, Structural and optical investigations of cobalt oxide nanoparticles, Exp. Theo. Nanotechnology (2021) 21–26, https://doi.org/10.56053/5.1.21.

[33] Y. Al-Douri (Ed.), Metal Oxide Powder Technologies: Fundamentals, Processing Methods and Applications, Elsevier Inc. ©, Netherlands, 2020.

[34] A. Bahrami, A. Delgado, C. Onofre, S. Muhl, S.E. Rodil, Structure, mechanical properties and corrosion resistance of amorphous Ti-Cr-O coatings, Surf. Coat. Technol. 374 (2019) 690–699, https://doi.org/10.1016/j.surfcoat.2019.06.061.

[35] S. He, A. Bahrami, X. Zhang, J. Julin, M. Laitinen, K. Nielsch, Low-temperature ALD of highly conductive antimony films through the reaction of silylamide with alkoxide and alkylamide precursors, Mater. Today Chem. 32 (2023), 101650, https://doi.org/10.1016/j.mtchem.2023.101650.

[36] A. Bahrami, C.F. Onofre Carrasco, A.D. Cardona, T. Huminiuc, T. Polcar, S.E. Rodil, Mechanical properties and microstructural stability of CuTa/Cu composite coatings, Surf. Coat. Technol. 364 (2019) 22–31, https://doi.org/10.1016/j.surfcoat.2019.02.072.

[37] J. Yang, A. Bahrami, X. Ding, P. Zhao, S. He, S. Lehmann, M. Laitinen, J. Julin, M. Kivekäs, T. Sajavaara, K. Nielsch, Low-temperature atomic layer deposition of high-k SbO_x for thin film transistors, Adv. Electron. Mater 8 (2022), 2101334, https://doi.org/10.1002/aelm.202101334.

[38] P. Doggali, F. Grasset, O. Cador, S. Rayalu, Y. Teraoka, N. Labhsetwar, Studies on catalytic and structural properties of $BaRuO_3$ type perovskite material for diesel soot oxidation, J. Environ. Chem. Eng. 2 (2014) 340–343, https://doi.org/10.1016/j.jece.2014.01.002.

[39] C. Dong, X. Yuan, X. Wang, X. Liu, W. Dong, R. Wang, Y. Duan, F. Huang, Rational design of cobalt–chromium layered double hydroxide as a highly efficient electrocatalyst for water oxidation, J. Mater. Chem. A 4 (2016) 11292–11298, https://doi.org/10.1039/C6TA04052G.

[40] J.D. Rodney, S. Deepapriya, M. Cyril Robinson, C. Justin Raj, S. Perumal, B.C. Kim, S. Jerome Das, Lanthanum doped copper oxide nanoparticles enabled proficient bi-functional electrocatalyst for overall water splitting, Int. J. Hydrogen Energy 45 (2020) 24684–24696, https://doi.org/10.1016/j.ijhydene.2020.06.240.

[41] S.A. Khalate, S.A. Kadam, Y.-R. Ma, S.S. Pujari, S.J. Marje, P.K. Katkar, A.C. Lokhande, U.M. Patil, Hydrothermally synthesized Iron Phosphate Hydroxide thin film electrocatalyst for electrocatalytic water splitting, Electrochim. Acta 319 (2019) 118–128, https://doi.org/10.1016/j.electacta.2019.06.162.

[42] B. Arunkumar, S. Johnson Jeyakumar, M. Jothibas, A sol-gel approach to the synthesis of CuO nanoparticles using Lantana camara leaf extract and their photo catalytic activity, Optik 183 (2019) 698–705, https://doi.org/10.1016/j.ijleo.2019.02.046.

[43] P. Kofstad, High-temperature oxidation of titanium, J. less-common met. 12 (1967) 449–464, https://doi.org/10.1016/0022-5088(67)90017-3.

[44] S.S. Kalanur, H. Seo, Intercalation of barium into monoclinic tungsten oxide nanoplates for enhanced photoelectrochemical water splitting, Chem. Eng. J. 355 (2019) 784–796, https://doi.org/10.1016/j.cej.2018.08.210.

[45] S.S. Kumbhar, M.A. Mahadik, P.K. Chougule, V.S. Mohite, Y.M. Hunge, K.Y. Rajpure, A.V. Moholkar, C.H. Bhosale, Structural and electrical properties of barium titanate ($BaTiO_3$) thin films obtained by spray pyrolysis method, Mater. Sci.-Pol 33 (2015) 852–861, https://doi.org/10.1515/msp-2015-0107.

[46] J. Balcerzak, W. Redzynia, J. Tyczkowski, In-situ XPS analysis of oxidized and reduced plasma deposited ruthenium-based thin catalytic films, Appl. Surf. Sci. 426 (2017) 852–855, https://doi.org/10.1016/j.apsusc.2017.07.248.

[47] A. Galal, H.K. Hassan, N.F. Atta, A.M. Abdel-Mageed, T. Jacob, Synthesis, structural and morphological characterizations of nano-Ru-based perovskites/RGO composites, Sci. Rep. 9 (2019) 7948, https://doi.org/10.1038/s41598-019-43726-1.

[48] Z. Huang, M. Wen, Q. Wu, Y. Zhang, H. Fang, H. Chen, Fabrication of Cu@AgCl nanocables for their enhanced activity toward the catalytic degradation of 4-chlorophenol, J. Colloid Interface Sci. 460 (2015) 230–236, https://doi.org/10.1016/j.jcis.2015.08.066.

[49] C. Liu, Y. Zhang, F. Dong, A.H. Reshak, L. Ye, N. Pinna, C. Zeng, T. Zhang, H. Huang, Chlorine intercalation in graphitic carbon nitride for efficient photocatalysis, Appl. Catal. B Environ. 203 (2017) 465–474, https://doi.org/10.1016/j.apcatb.2016.10.002.

[50] M. Li, F. Bi, Y. Xu, P. Hao, K. Xiang, Y. Zhang, S. Chen, J. Guo, X. Guo, W. Ding, Effect of residual chlorine on the catalytic performance of Co_3O_4 for CO oxidation, ACS Catal. 9 (2019) 11676–11684, https://doi.org/10.1021/acscatal.9b03797.

[51] K.H. Kwak, D.W. Kim, Y. Kang, J. Suk, Hierarchical Ru-and RuO_2-foams as high performance electrocatalysts for rechargeable lithium–oxygen batteries, J. Mater. Chem. A 4 (2016) 16356–16367, https://doi.org/10.1039/C6TA05077H.

[52] R. Zhang, C. Tang, R. Kong, G. Du, A.M. Asiri, L. Chen, X. Sun, Al-Doped CoP nanoarray: a durable water-splitting electrocatalyst with superhigh activity, Nanoscale 9 (2017) 4793–4800, https://doi.org/10.1039/C7NR00740J.

[53] L. Yang, Z. Guo, J. Huang, Y. Xi, R. Gao, G. Su, W. Wang, L. Cao, B. Dong, Vertical growth of 2D amorphous $FePO_4$ nanosheet on Ni foam: outer and inner structural design for superior water splitting, Adv. Mater. 29 (2017), 1704574, https://doi.org/10.1002/adma.201704574.

[54] R.M. Ramsundar, J. Debgupta, V.K. Pillai, P.A. Joy, Co_3O_4 nanorods—efficient non-noble metal electrocatalyst for oxygen evolution at neutral pH, Electrocatalysis 6 (2015) 331–340, https://doi.org/10.1007/s12678-015-0263-0.

[55] L. Kumar, B. Antil, A. Kumar, M.R. Das, S. Deka, A superior and stable electrocatalytic oxygen evolution reaction by one-dimensional FeCoP colloidal nanostructures, ACS Appl. Mater. Interfaces 14 (2022) 5468–5477, https://doi.org/10.1021/acsami.1c23014.

[56] A.T. Swesi, J. Masud, M. Nath, Nickel selenide as a high-efficiency catalyst for oxygen evolution reaction, Energy Environ. Sci. 9 (2016) 1771–1782, https://doi.org/10.1039/C5EE02463C.

[57] R. Samanta, P. Panda, R. Mishra, S. Barman, IrO_2-Modified RuO_2 nanowires/nitrogen-doped carbon composite for effective overall water splitting in all pH, Energy Fuel. 36 (2022) 1015–1026, https://doi.org/10.1021/acs.energyfuels.1c04082.

[58] Y. Fan, X. Zhang, Y. Zhang, X. Xie, J. Ding, J. Cai, B. Li, H. Lv, L. Liu, M. Zhu, X. Zheng, Decoration of Ru/RuO_2 hybrid nanoparticles on MoO_2 plane as bifunctional electrocatalyst for overall water splitting, J. Colloid Interface Sci. 604 (2021) 508–516, https://doi.org/10.1016/j.jcis.2021.07.038.

[59] Y. Pei, S. Guo, Q. Ju, Z. Li, P. Zhuang, R. Ma, Y. Hu, Y. Zhu, M. Yang, Y. Zhou, J. Shen, Interface engineering with ultralow ruthenium loading for efficient water splitting, ACS Appl. Mater. Interfaces 12 (2020) 36177–36185, https://doi.org/10.1021/acsami.0c09593.

[60] B. Tang, X. Yang, Z. Kang, L. Feng, Crystallized $RuTe_2$ as unexpected bifunctional catalyst for overall water splitting, Appl. Catal. B Environ. 278 (2020), 119281, https://doi.org/10.1016/j.apcatb.2020.119281.

[61] S. Nong, W. Dong, J. Yin, B. Dong, Y. Lu, X. Yuan, X. Wang, K. Bu, M. Chen, S. Jiang, L.M. Liu, Well-dispersed ruthenium in mesoporous crystal TiO_2 as an advanced electrocatalyst for hydrogen evolution reaction, J. Am. Chem. Soc. 140 (2018) 5719–5727, https://doi.org/10.1021/jacs.7b13736.

[62] S.M. Galani, A. Mondal, D.N. Srivastava, A.B. Panda, Development of RuO_2/CeO_2 heterostructure as an efficient OER electrocatalyst for alkaline water splitting, Int. J. Hydrogen Energy 45 (2020) 18635–18644, https://doi.org/10.1016/j.ijhydene.2019.08.026.

[63] H. Liu, G. Xia, R. Zhang, P. Jiang, J. Chen, Q. Chen, MOF-derived RuO_2/Co_3O_4 heterojunctions as highly efficient bifunctional electrocatalysts for HER and OER in alkaline solutions, RSC Adv. 7 (2017) 3686–3694, https://doi.org/10.1039/C6RA25810G.

[64] Z. Ding, K. Wang, Z. Mai, G. He, Z. Liu, Z. Tang, RhRu alloyed nanoparticles confined within metal organic frameworks for electrochemical hydrogen evolution at all pH values, Int. J. Hydrogen Energy 44 (2019) 24680–24689, https://doi.org/10.1016/j.ijhydene.2019.07.244.